Research Square

Preprints are preliminary reports that have not undergone peer review.
They should not be considered conclusive, used to inform clinical practice,
or referenced by the media as validated information.

Biochar-supported Fe/Mg co-doped MoS_2 synergistically enhances PMS activation for the degradation of tetracycline hydrochloride: A study on the Fe^{2+}/Fe^{3+} cycling driving mechanism and catalytic stability

Haifeng Li
Shanghai Polytechnic University
Yu Yao
Shanghai Polytechnic University
Peixuan Li
Shanghai Polytechnic University
Xiqian Guo
Shanghai Polytechnic University
Yan Zhang
yzhang@sspu.edu.cn
Shanghai Polytechnic University
Jifen Wang
Shanghai Polytechnic University
Yi Zhang
Shanghai Polytechnic University

Research Article

Keywords: Tetracycline Hydrochloride (TCH), Advanced Oxidation Process with Peroxymonosulfate (PS-AOPs), Fe^{2+}/Fe^{3+} Cycling, Stability

Posted Date: September 22nd, 2025

DOI: https://doi.org/10.21203/rs.3.rs-7582872/v1

License: This work is licensed under a Creative Commons Attribution 4.0 International License.
Read Full License

Additional Declarations: No competing interests reported.

Biochar-supported Fe/Mg co-doped MoS_2 synergistically enhances PMS activation for the degradation of tetracycline hydrochloride: A study on the Fe^{2+}/Fe^{3+} cycling driving mechanism and catalytic stability

Haifeng Li[1], Yu Yao[1], Peixuan Li[1], Xiqian Guo[1], Yan Zhang[1]*, Jifen Wang[1]* and Yi Zhang[1].

Abstract

Due to its high efficiency, safety, and low economic cost, peroxymonosulfate (PMS) advanced oxidation processes (AOPs) are widely used for removing organic pollutants from wastewater. In this study, an environmentally friendly porous biochar was prepared from waste wood powder generated in the building materials industry through simple pyrolysis, and iron-magnesium oxide with high catalytic activity, stability, and low cost was loaded as the active center. Mo ions were added to create a ternary composite catalyst. At room temperature, a 0.5 g/L catalyst concentration and 5 mM PMS achieved a 98.22% removal of 20 mg/L tetracycline hydrochloride within 2 minutes, with complete degradation occurring within 60 minutes. The catalytic degradation rate exceeded 93.76% across a pH range of 3-10, demonstrating broad pH adaptability. Recycle tests showed that the degradation rate of tetracycline hydrochloride was 87.38% after 9 cycles, confirming the catalyst's recyclability and reusability. This addresses the current challenge of low catalyst utilization, enabling the efficient removal of organic pollutants quickly while reducing production costs and process time. The high catalytic performance, recyclability, wide pH range, and low ion leaching rate of the catalyst in antibiotic wastewater treatment highlight its broad application potential as a PMS activator, offering a new approach to catalyst design for advanced oxidation degradation of antibiotic pollutants PMS.

Haifeng Li
20241516043@sspu.edu.cn

Yu Yao
20241516134@sspu.edu.cn

Peixuan Li
20231516034@sspu.edu.cn

Xiqian Guo
q7099778@163.com

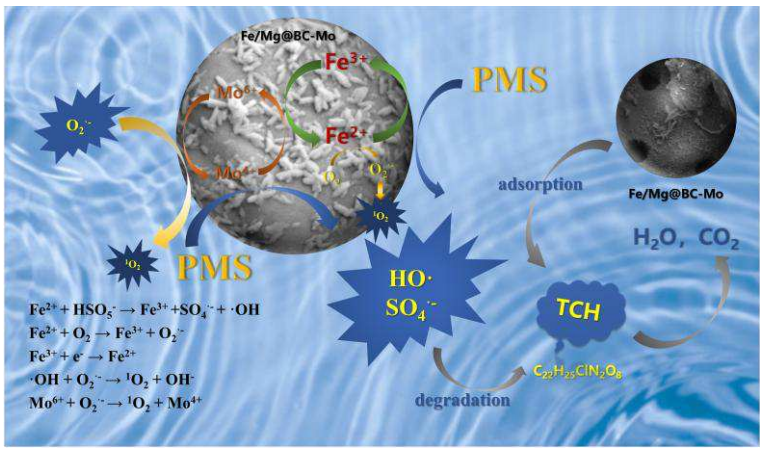
Yan Zhang
yzhang@sspu.edu.cn

Jifen Wang
wangjifen@sspu.edu.cn

Yi Zhang
18721162696@163.com

[1] School of Resources and Environmental Engineering, Shanghai Polytechnic University, 2360 Jinhai Road, Pudong New Area, Shanghai, China

Graphical Abstract



Keywords Tetracycline Hydrochloride (TCH); Advanced Oxidation Process with Peroxymonosulfate (PS-AOPs); Fe^{2+}/Fe^{3+} Cycling; Stability

Abbreviations

TCH	Tetracycline Hydrochloride
TC	Tetracycline
PMS/PDS	Peroxymonosulfate/Peroxydisulfate
EPR	Electron paramagnetic resonance
XPS	X-ray photoelectron spectroscopy
LC-MS	Liquid chromatography-mass spectrometry
BET	Brunauer-Emmett-Teller
FTIR	Fourier transform infrared spectroscopy
XRD	X-ray diffraction
LSV	Linearity sweep voltammetry
I-t	Current-time
SEM	Electron microscopy
EDS	Energy-Dispersive X-ray Spectroscopy
L-His	L-histidine
ρ-BQ	ρ-benzoquinone
TBA	Tert-butanol
MeOH	Methanol
PS-AOPs	Advanced Oxidation Process with Peroxymonosulfate
ICP-AES	Inductively coupled plasma atomic emission spectroscopy

1. Introduction

The global consumption of antibiotics continues to increase**[1]**. Tetracycline hydrochloride, due to its low cost and easy availability, is widely added to animal feed in agriculture and animal husbandry to treat bacterial infections in animals and promote their growth**[2]**. However, due to the incomplete metabolic profiles of antibiotics in organisms, a significant portion is excreted in their original form into the environment, leading to widespread pollution of soil and aquatic ecosystems**[3]**. Because of its unique physicochemical properties (including its persistence in water environments and high solubility) and its significant ecological risks, it has become a key focus of water pollution control.

As global concerns regarding water environmental safety and ecological health continue to intensify, the current treatment approaches for tetracycline pollutants can be categorized into the following classifications: physical adsorption technology**[4]-[6]**, chemical oxidation technology**[7]-[9]**, biodegradation technology**[10]-[11]**, and advanced oxidation processes (AOPs)**[12]**. Among them, Advanced persulfate oxidation technology (SR-AOPS) causes the breaking of the peroxide bond (O-O) in persulfate (PMS/PDS) molecules through various activation methods, thereby generating highly reactive free radicals and non-free radical species, including sulfate radical ($SO_4^{\cdot-}$), hydroxyl radical (·OH), superoxide radical ($O_2^{\cdot-}$), and singlet oxygen ($^1O_2$)**[13]**. These reactive species possess powerful oxidising ability and can efficiently break down organic pollutants in water bodies. Compared with traditional Fenton oxidation technology, SR-AOPS based on $SO_4^{\cdot-}$ displays notable advantages, such as a higher oxidation-reduction potential ($SO_4^{\cdot-}$ E_0 = 2.5-3.1 V) compared to ·OH (E_0 = 2.7 V, $t_{1/2}$ ⩽ 1 μs), a longer half-life ($t_{1/2}$ = 30-40 μs), and a wider pH application range (pH 2-9)**[14]**, giving it significant potential in water treatment. Currently, activation methods of persulfate include thermal activation, alkaline activation, photoactivation, and transition metal activation strategies: 1) Thermal activation**[15]**: By heating (usually > 50 °C) to provide energy, persulfate molecules are cleaved to produce $SO_4^{\cdot-}$. 2) Alkaline activation**[16]-[17]**: Persulfate can decompose to produce various reactive oxygen species (such as ·OH, $O_2^{\cdot-}$) under conditions of pH > 10. 3) Photoactivation**[18]**: Persulfate absorbs photon energy to form an excited state ($S_2O_8^{2-}$), which then cleaves to produce $SO_4^{\cdot-}$. 4) Transition metal activation**[19]**: Transition metal ions such as iron (Fe^{2+}/Fe^{3+}), copper (Cu^{+}/Cu^{2+}), and manganese (Mn^{2+}), among others, can effectively activate persulfate through electron transfer, offering the benefits of simple operation and low cost, and have recently become a focus of research.

Transition metal ions such as Ni^{2+}, Co^{2+}, Mn^{2+}, and Ag^{+} commonly catalyse persulfate. Although Co^{2+} and Ag^{+} have strong activation abilities for PDS/PMS**[20]**, they possess specific toxicity and may pose risks of secondary pollution. In contrast, iron not only exhibits a strong activation ability for

PMS**[21]**-**[22]**, but is also low-cost, abundant, and non-toxic. It is a widely used metal for activating PMS to degrade organic pollutants. Currently, nano-zero-valent iron (nZVI)**[21]** is extensively employed in organic pollutant degradation research due to its high surface area and strong reduction capacity. However, nZVI tends to aggregate and encounter issues such as decreased catalytic efficiency**[23]**. To address this issue, the study uses biochar (BC) as a support material. It introduces Mg^{2+}, known for its high solubility and eco-friendly properties, through the impregnation-thermal decomposition method to form a stable iron-magnesium-oxygen structure that is evenly dispersed on the carrier's surface. The iron-magnesium-oxygen structure as a whole exhibits strong magnetism**[24]**, enabling rapid separation and recovery of the catalyst under an external magnetic field, which addresses the challenge of difficult separation associated with traditional catalysts. Additionally, the iron-magnesium-oxygen structure is stable and possesses certain acid-base resistance, reducing issues related to Fe^{2+} regeneration difficulties and iron ion leaching in the practical application of iron-based biochar catalysts**[25]**-**[26]**. However, catalysts prepared by this method have less Fe^{2+} on their surface, with most metal iron ions existing as Fe^{3+}, which exhibits poor reducibility and low catalytic activity. Recent research has shown**[27]**-**[28]** that adding metal ions such as Co^{2+}, Mn^{2+} and Cu^{+} can accelerate the regeneration cycle of Fe^{2+}, thereby improving catalytic efficiency. Molybdenum disulfide (MoS_2) has numerous active centres and a strong affinity for PMS, which enhances electron transfer**[29]**-**[30]** and aids in breaking the peroxide bond (O-O), producing $SO_4^{\cdot-}$ and ·OH free radicals. Moreover, due to its high electron mobility, it can act as a co-catalyst to accelerate the regeneration cycle of Fe^{2+}/Fe^{3+}. Consequently, incorporating Mo in this study aims to improve the dispersion of the metal oxide structure, strengthen the interaction between metal and carrier to prevent metal ion aggregation**[31]**, accelerate the reduction and regeneration of Fe^{3+}, and ultimately boost catalytic efficiency and the recycling and regeneration capacity of the catalysts.

The experimental study examined the preparation process, pore structure, and surface chemical bond distribution of the catalyst Fe/Mg@BC-Mo. It also assessed the catalytic performance, stability, and degradation efficiency in conditions simulating actual wastewater environments. Using techniques such as electron paramagnetic resonance (EPR), electrochemical testing, X-ray photoelectron spectroscopy (XPS), and liquid chromatography-mass spectrometry (LC-MS), multi-dimensional synergy was employed to uncover the degradation mechanism of TCH by the Fe/Mg@BC-Mo/PMS system and to hypothesise the degradation pathway. The study monitored metal leaching concentrations and evaluated environmental safety. It aimed to facilitate the recycling of metal ions (Fe^{2+}/Fe^{3+}), improve electron transfer capabilities to activate PMS efficiently for TCH degradation, and increase catalyst recyclability through magnetic components, enabling rapid magnetic separation and recovery. This research provides a new theoretical foundation and technical support for the application of PMS-based advanced oxidation technology in treating actual antibiotic wastewater.

2. Experimental section

2.1. Chemicals and Reagents

Text S1 of the Supporting Information provides a complete list of reagents.

2.2. Experimental Procedure

Preparation of Fe/Mg@BC-Mo (Fig. 1a): The wood powder from crushed wood was carbonised under nitrogen at 700 °C for 1 hour, then sieved through a 100-mesh screen, washed with 1M HCl to remove ash, and vacuum-filtered with deionised water until neutral pH. The treated biochar powder was dried at 80 °C for 3 hours. A mixed solution of $FeSO_4 \cdot 7H_2O$ and $MgSO_4$ was prepared in a molar ratio of 2:1 and stirred with the pre-treated biochar for 1 hour for complete mixing, followed by impregnation for 24 hours. The mixture was then vacuum-filtered, washed to a neutral pH, and dried at 80 °C for 3 hours. After grinding with MoS_2 in a 1:1 (wt%) ratio until homogeneous, it was pyrolysed under nitrogen at 500 °C for 1 hour to obtain the catalyst. Catalysts Fe@BC, Mg@BC, and Fe/Mg@BC were prepared using the same method.

The reaction temperature was maintained at room temperature (25 °C), while magnetic stirring was set at 300 rpm. An initial TCH concentration of 20 mg/L was used, along with 5 mM PMS and a catalyst dosage of 0.5 g/L, with a reaction time of 1 hour, to examine the effects of various catalytic systems on pollutant degradation (Text S2). Furthermore, different amounts of MoS_2, catalyst dosage, and simulated anionic concentrations in natural water bodies were varied to evaluate the degradation effectiveness of the catalyst (Text S3). The Fe/Mg@BC-Mo catalyst was collected through vacuum filtration, washed with ultrapure water, and dried for recycling. All experiments were repeated multiple times, with three parallel groups established for each experiment. The results are presented as averages.

2.3. Analytical Methods

Scanning electron microscopy and energy dispersive X-ray spectroscopy (SEM-EDS, S-48DD, Japan) were employed to examine the morphological features of BC, Fe/Mg@BC, and Fe/Mg@BC-Mo, as well as to analyse the elemental composition on the catalyst surface. Brunauer-Emmett-Teller (BET, MicritracBel, Bel sorp-max, USA) was used to assess the catalysts' pore structure and specific surface area. Fourier transform infrared spectroscopy (FTIR, Thermo Fisher Nicolet iS20) was utilised to identify the chemical bonds within the catalysts. The Raman spectrometer (SENTERRA) was employed to evaluate the structural defects in the carbon materials. X-ray diffraction (XRD, Bruker D8 ADVANCE, Germany) was used to determine the catalysts' crystal structure and phase composition within the 2θ range of 10° to 80°. Liquid chromatography-mass spectrometry (Shimadzu LCMS-8040, Japan) was used for quantitative analysis of TCH concentration during degradation and qualitative analysis of the molecular weight and structure of degradation intermediates(Text S4). X-ray photoelectron spectroscopy (XPS, Thermo Fisher-VG Scientific) was employed to assess changes in surface composition and elemental content of the catalyst before and after use. Electron paramagnetic resonance (EPR) spectroscopy

was utilised to measure $SO_4^{\cdot-}$, ·OH, and $^1O_2$ generated in the reaction system. Linearity sweep voltammetry (LSV) and current-time (I-t) curves, conducted with an electrochemical analyser, elucidated the degradation mechanism of TCH in the Fe/Mg@BC-Mo/PMS system. Inductively coupled plasma atomic emission spectroscopy (ICP-AES) was employed to determine the concentrations of metal ions.

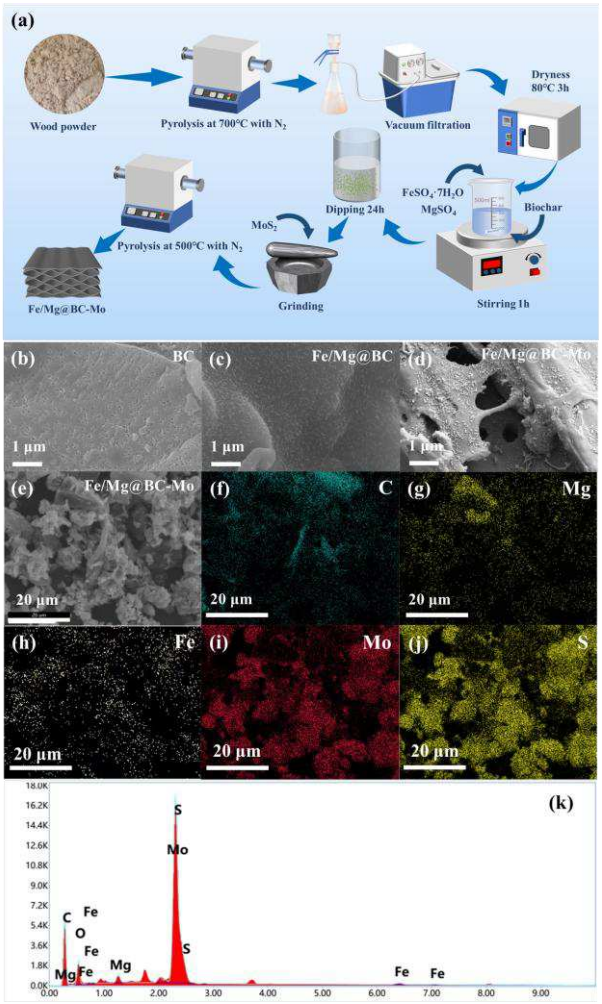


Fig.1 (a) Schematic diagram of the preparation process for Fe/Mg@BC-Mo; (b) BC; (c) Fe/Mg@BC; (d) Fe/Mg@BC-Mo; (e) EDS image of Fe/Mg@BC-Mo; (f-j) Element mapping images of Fe/Mg@BC-Mo; (k) Element distribution map of Fe/Mg@BC-Mo after surface scanning.

3. Results and discussion

3.1. Characterisation

The surface morphology of the catalysts BC, Fe/Mg@BC, and Fe/Mg@BC-Mo was examined using scanning electron microscopy (SEM), as shown in Fig. 1. The surface of the biochar BC (Fig. 1b) appeared relatively flat and smooth with uniform and dense pore structures, which resulted from the release of volatile substances during thermal decomposition, leading to the formation of numerous pores in BC. The biochar Fe/Mg@BC (Fig. 1c) displayed a surface covered with a large amount of light-coloured crystalline structures, consistent with the literature**[26]**. Based on the XRD results, it was inferred that these crystals were compounds formed by the reaction of Fe and Mg ions with functional groups or other components on the biochar surface. With successful loading of metal ions, the surface voids of the catalyst substrate were filled with metal ions or their resulting compounds. Under SEM, the Fe/Mg@BC-Mo catalyst (Fig. 1d) exhibited an evident surface pore structure, characterised by irregular and uniformly attached small particles. This indicated that the addition of MoS_2 promoted a uniform dispersion of metal oxides and increased microporosity, which could provide more active sites for PMS activation. EDS scanning on Fe/Mg@BC-Mo revealed that elements Fe, Mg, and Mo were evenly distributed across the catalyst surface; notably, the Mg content was higher. Correlating this with subsequent XRD findings, it is likely due to the presence of $CaMg(CO_3)_2$ in the bio-based substrate wood powder**[32]-[33]**.

To clarify the phase structure of the sample, X-ray diffraction (XRD) was used to characterise the sample (Fig. 2a). The XRD pattern of BC showed a large amount of $CaMg(CO_3)_2$ in the biochar substrate, with sharp diffraction peaks at 2θ = 30.9°, confirming the higher Mg element result obtained from EDS scanning. The XRD patterns of Fe/Mg@BC and Fe/Mg@BC-Mo displayed sharp diffraction peaks at 2θ = 45.2° and 65.1°, indexed as Fe_3C, and a diffraction peak for MgO at 2θ = 36.8°. Diffraction peaks of $MgFe_2O_4$ appeared at 2θ = 42.7° and 62.0°, indicating the formation of a complex iron-magnesium oxide crystal structure**[34]**. These results suggest that Fe and Mg were successfully attached to the biochar substrate. However, the intensity of $MgFe_2O_4$ decreased after Mo doping, implying that the uniform dispersion of MoS_2 hindered metal particle aggregation. Fourier transform infrared spectroscopy (FTIR) was used to further analyse the surface functional groups of the catalyst (Fig. 2b). The absorption peak at 3445 cm^{-1} was characteristic of hydroxyl (-OH)**[35]**. Additionally, the peak at 2379 cm^{-1} corresponded to the C=O bond**[36]**, while the stretching vibration peaks of carboxyl (-COOH) at 1624 cm^{-1} and 1427 cm^{-1} indicated that numerous functional groups appeared on the catalyst surface after thermal treatment and acid washing **[37]-[38]**. These groups could improve pollutant adsorption and offer more active sites for electron transfer, thereby boosting the reaction rate. The abundant hydroxyl, carboxyl, and other functional groups could form stable coordination bonds with Fe and Mg metal ions, enabling the metal ions to be firmly attached to the biochar surface and enhancing the stability, service life, and reusability of the catalyst. Meanwhile, the coordination interactions between these functional groups and metal ions prevented Fe and Mg ions from aggregating during high-temperature pyrolysis, ensuring their uniform dispersion on the catalyst surface. Characteristic peaks at 625 cm^{-1} and 450 cm^{-1} are attributed to the stretching vibration of Fe-O-Fe or Mg-O bonds and the bending vibration of M-O-C bonds, further confirming that Fe and Mg metal ions were successfully and stably anchored to the surface of the biochar**[26]**,**[39]**.

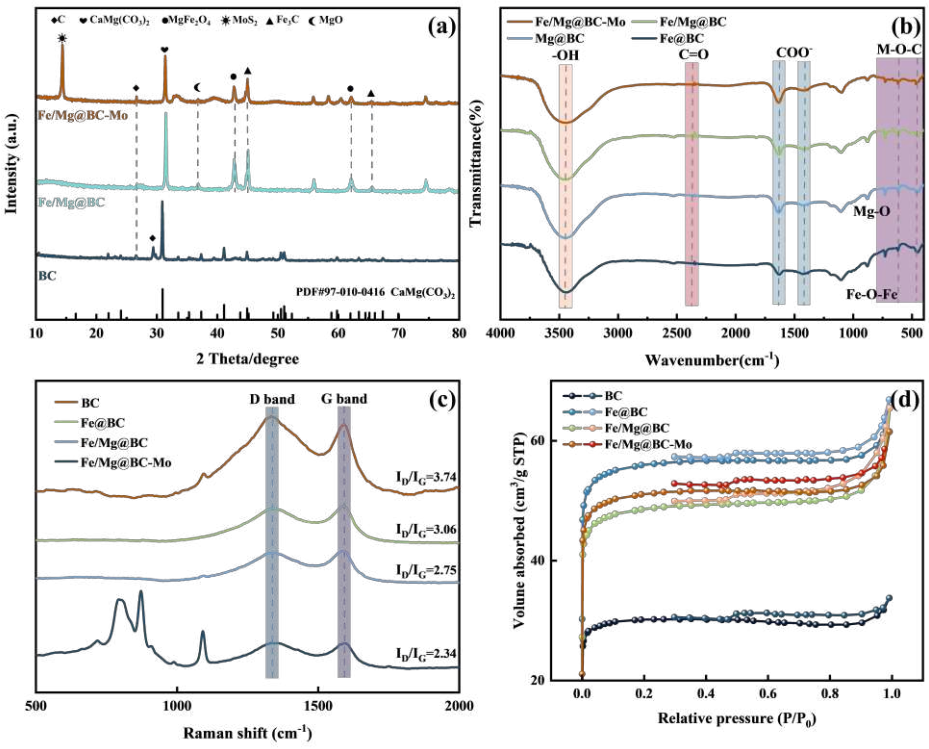


Fig.2 (a) XRD spectrum; (b) FTIR spectrum; (c) Raman spectrum; and (d) N_2 adsorption-desorption curve obtained from Brunauer-Emmett-Teller analysis.

Fig. 2c displays the Raman spectrum of the catalytic material. According to references **[3]**,**[40]**, porous carbon materials exhibit prominent D and G peaks at 1350 cm^{-1} and 1580 cm^{-1}, which relate to the extent of lattice carbon defects and the graphite carbon content of the material**[41]**. The ratio of the intensities of these two peaks, known as the peak height or area ratio (I_D/I_G), indicates the level of defects in the carbon material. A higher I_D/I_G value signifies a greater presence of defective carbon and a lower degree of graphitisation. The I_D/I_G value of the biochar after loading iron-magnesium oxides and introducing Mo decreased from 3.47 to 2.34, suggesting that the edge sites and functional groups of the original biochar increased during high-temperature pyrolysis**[42]**, resulting in a higher degree of carbon defects. After metal modification, the metal ions reacted with surface functional groups and formed uniform oxide attachments, altering the distribution of active sites and promoting the graphiteification of carbon. The Brunauer-Emmett-Teller (BET) test was used to analyse the pore characteristics and specific surface area of the catalyst. As shown in Fig. 2d, the N_2 adsorption-desorption curves for BC, Fe@BC, Fe/Mg@BC, and Fe/Mg@BC-Mo all display clear IV-type adsorption-desorption isotherms**[3]**,characterisedd by H4 type narrow slit-like lagging rings. The pore size distribution in the catalytic material is broad, consisting of both micropores and mesopores. The micropore content of the catalyst components loaded with metal ions significantly increases compared with BC. Based on Table S1, the BET specific surface area and pore characteristics of BC, Fe@BC, Fe/Mg@BC， and Fe/Mg@BC-Mo show that the specific surface area rises from 124.20 $m^2 \cdot g^{-1}$ to 205.91 $m^2 \cdot g^{-1}$, and the total pore volume increases from 0.0520 $cm^3 \cdot g^{-1}$ to 0.0942 $cm^3 \cdot g^{-1}$. Compared to BC, the specific surface area and total pore volume of Fe@BC, Fe/Mg@BC， and Fe/Mg@BC-Mo nearly double. The specific surface area, micropore specific surface area, and pore volume in the Fe/Mg@BC component all demonstrate the best performance. This may be because the metal ions Fe and Mg act more effectively as "porogens" during the high-temperature pyrolysis process, catalyzing the gasification reaction of the biochar's carbon framework to produce more micropores or mesopores**[43]**. In the Fe/Mg@BC-Mo sample, the high metal loading causes the metal compounds to penetrate or cover the biochar pores during pyrolysis, leading to blockage. Simultaneously, the high loading of MoS_2 and iron-magnesium oxide crystals reduces the specific surface area**[44]**. In summary, the BET results suggest that the modified Fe/Mg@BC-Mo possesses a large specific surface area and a rich pore structure, which is beneficial for the adsorption of tetracycline hydrochloride salt and provides more active sites for PMS activation.

3.2. Catalytic Performance Evaluation

3.2.1. The Effect of Various Catalytic Systems on TCH Degradation

By activating PMS to degrade TCH, the catalytic degradation performance of different catalysts BC, Fe@BC, Fe/Mg@BC, and Fe/Mg@BC-Mo was examined. As shown in Fig. 3a, the biochar BC produced by simple pyrolysis and carbonisation could not degrade pollutants due to its rich pore structure and large specific surface area, but it had a certain adsorption effect on contaminants, with an

adsorption efficiency of 43.96% within 60 minutes. After acid washing and loading metal ions, the removal rates of TCH by the catalyst systems Fe@BC, Mo@BC, and Fe/Mg@BC within 2 minutes were 30.79%, 3.34%, and 56.37%, respectively, and the degradation rates at 60 minutes were 59.00%, 69.33%, and 83.15%, respectively. Due to the possible oxidation of Fe ions during the impregnation-thermal decomposition process, which diminishes the activation of PMS, the addition of Mg ions can enhance electron transfer and thereby improve the degradation effect. However, in the current literature, issues remain with the low recycling utilisation of bimetallic-loaded catalysts**[26]**,**[45]**. To address this, Mo was introduced to strengthen the cycling of iron valence states, further improving the pollutants' degradation efficiency while increasing the catalyst's recycle utilisation. The degradation efficiency of TCH by the catalyst Fe/Mg@BC-Mo within 2 minutes reached 98.22%, with pollutants being completely degraded within 60 minutes. The degradation effects of each group indicated that Fe and Mo ions had a synergistic enhancement during the reaction process.

3.2.2. Factors Influencing TCH Degradation in the Fe/Mg@BC-Mo/PMS System

As shown in Fig. 3b, when the initial TCH concentration was 10, 20, 30, 50, and 80 mg/L, the degradation rates of TCH by the catalytic system within 2 minutes were 95.88%, 98.22%, 95.28%, 94.90%, and 94.75%, respectively. The removal rates reached over 98% within 60 minutes. This is because the Fe^{2+} on the catalyst surface activates PMS through single electron transfer to generate highly active sulfate and hydroxyl radicals, and it is oxidised to Fe^{3+}. Fe^{3+} can also exhibit reducing properties under certain conditions, but its strong oxidising property is comparatively weaker. The doping of Mo effectively promotes the cycling of iron valence states, and the Mo^{4+} on the catalyst surface can provide electrons for Fe^{3+} to facilitate the reduction and regeneration of Fe^{2+}, enabling Fe^{2+} to continuously activate PMS to generate highly active free radicals for the degradation of TCH. In addition, MoS_2 can also activate PMS to produce a large number of free radicals**[46]**.

Fig. 3c examined the impact of catalyst dosage on the degradation of TCH by the catalytic system. The results demonstrated that reducing the catalyst dosage to 0.01 g/L achieved a removal efficiency of 95.29% within 2 minutes. The degradation outcomes showed that as the catalyst dosage increased from 0.01 g/L to 0.5 g/L, more catalysts provided additional active sites to activate PMS, thus generating highly active free radicals to break down TCH. Consequently, the TCH removal rate displayed a steady increase. However, at a relatively high dosage of 0.5 g/L, no over-limit Fe^{2+} effect on the free radicals already produced in the system was observed, as reported in many current studies. **[47]-[48]** Macroscopically, the degradation efficiency of the catalyst system at high dosage decreased, which has been explained in literature as excess Fe^{2+} consuming some free radicals, leading to a reduction in the concentration of highly active free radicals involved in pollutant degradation and thus hampering the process. Considering the abundant hydroxyl and carboxyl functional groups on the catalyst surface, along with the rich pore structure and large specific surface area of biochar itself, it is speculated that these surface functional groups may dissociate and electrostatically adsorb Fe^{2+} from the solution, or react with initial cations such as Mg^{2+} on the catalyst surface via ion exchange, re-fixing on the biochar surface.

Fig. 3d investigated the effect of different initial pH levels on TCH degradation. When the pH was adjusted to 3, 5, 7, and 10, pollutant removal was observed within 60 minutes. The results indicated that degradation rates within 2 minutes were 88.70%, 94.36%, 94.34%, and 94.95%, respectively. At pH=3, the total removal rate reached 93.76% after 60 minutes, while the other groups achieved removal rates above 96%. The reaction was slightly inhibited under strongly acidic conditions, consistent with the literature**[49]**, which suggests that high concentrations of H^+ ions can inhibit $SO_4^{\cdot-}$ and $^1O_2$. Under weak acidic conditions, the natural pH exhibited the best catalytic performance. Acidic conditions favoured the stability of Fe^{2+} and the activation of PMS, and MoS_2 maintained good chemical stability in weakly acidic and weakly alkaline environments, reducing Mo^{4+} loss and facilitating participation in the activation reaction**[31]**. According to report**[50]**, weak alkaline conditions promote the formation of ·OH and help protect the catalyst's surface crystallinity, effectively preventing metal leaching into the reaction solution and thereby increasing PMS induced $SO_4^{\cdot-}$ generation. This is confirmed by the removal rate of 94.95% within 2 minutes at pH=10. Based on these findings, the Fe/Mg@BC-Mo/PMS catalytic system exhibits adaptability over a wide pH range.

By simulating the presence of various anions in real wastewater, the effects of common coexisting ions such as Cl^-, CO_3^{2-}, $H_2PO_4^-$, and anionic surfactants like sodium dodecylbenzenesulfonate (SDBS) and humic acid (HA) on the degradation of TCH by the Fe/Mg@BC-Mo/PMS system were investigated**[51]**. As shown in Fig. 3e, the removal rates of TCH by the catalytic system within 2 minutes were 89.26%, 86.95%, and 88.08% for the CO_3^{2-}, $H_2PO_4^-$, and SDBS groups, respectively, and the degradation rates within 60 minutes were 92.99%, 94.14%, and 94.19% respectively. The effect of humic acid (HA) on the catalytic system was minimal, confirming the system's adaptability over a broad pH range. Additionally, Cl^- slightly inhibited the catalytic system, with degradation rates of 93.05% and 93.60% at 2 minutes and 60 minutes, respectively, and the degradation rate plateaued over time, due to the reaction between Cl^- and free radicals, as shown in Equations (1) and (2). $H_2PO_4^-$ has a strong capacity to adsorb transition metals and can form insoluble phosphate compounds such as $FePO_4$ with Fe^{3+}, reducing the active centres of the catalyst and negatively affecting TCH degradation, as shown in Equation (3). Furthermore, CO_3^{2-} and $H_2PO_4^-$ can participate in hydrogen transfer or redox reactions with the highly reactive hydroxyl radical ·OH and sulfate radical $SO_4^{\cdot-}$, as shown in Equations (4) - (6), significantly reducing the reactive oxygen species (ROS) in the system and thus inhibiting degradation.

$$Cl^- + SO_4^{\cdot-} \rightarrow SO_4^{2-} + Cl\cdot \quad (1)$$

$$Cl^- + \cdot OH \rightarrow ClOH^{\cdot-} \quad (2)$$

$$3H_2PO_4^- + Fe^{3+} \rightarrow FePO_4 + 4H^+ + 2H_2O \quad (3)$$

$$CO_3^{2-} + SO_4^{\cdot-} \rightarrow SO_4^{2-} + CO_3^{\cdot-} \quad (4)$$

$$\cdot OH + H_2PO_4^- \rightarrow H_2O + PO_3^{\cdot 3-} \quad (5)$$

$$SO_4^{\cdot-} + H_2PO_4^- \rightarrow H_2O + PO_3^{\cdot 3-} + SO_4^{2-} \quad (6)$$

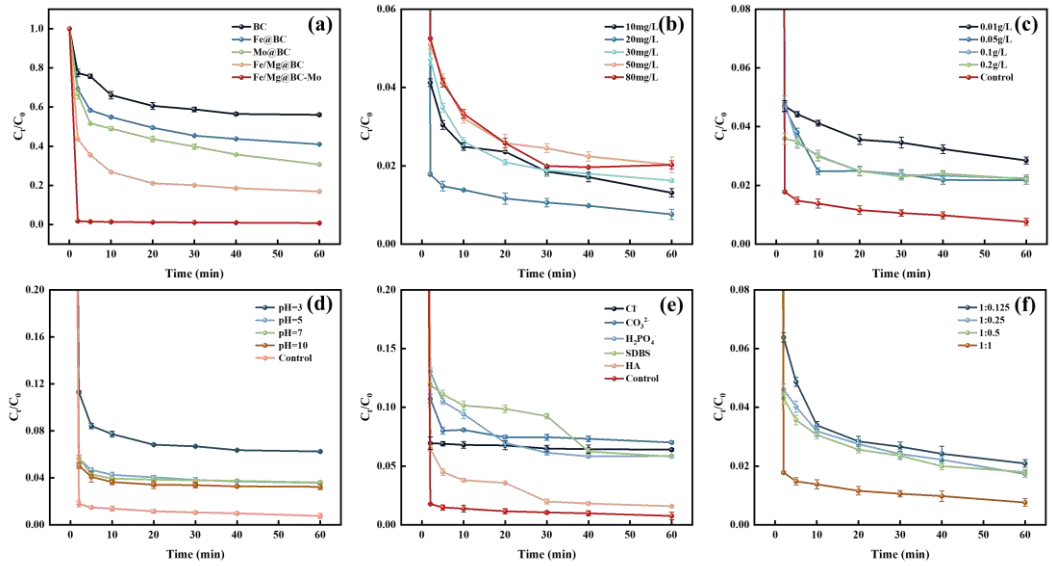


Fig.3 (a) Effects of different catalyst systems; (b) Initial TCH concentration; (c) Catalyst dosage, (d) Initial pH; (e) Inorganic anions; and (f) MoS_2 doping amount on the removal efficiency of TCH. Experimental conditions: $[PMS]_0$ = 5 mM, $[TCH]_0$ = 20 mg/L, $[Catalyst.]_0$ = 0.5 g/L, T = 25 °C, ambient pH, reaction time = 60 min.

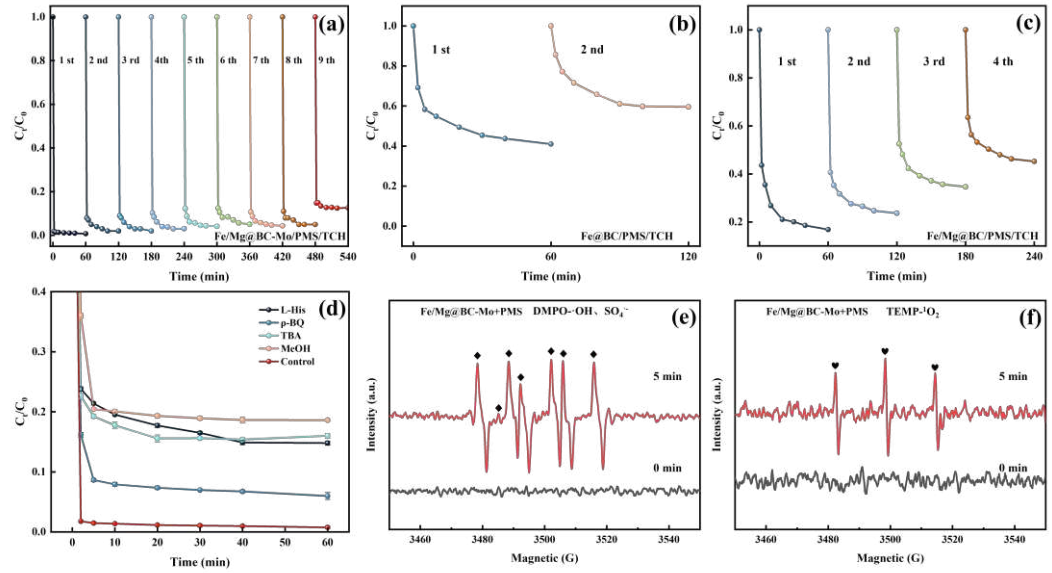


Fig.4 (a) Fe/Mg@BC-Mo/PMS; (b) Fe@BC/PMS; and (c) Fe/Mg@BC/PMS systems for cyclic removal of TCH. (d) Free radical quenching identification; (e) DMPO-$SO_4^{\cdot-}$ and DMPO-·OH; (f) EPR spectra of TEMP-$^1O_2$.Experimental conditions: $[PMS]_0$ = 5 mM, $[TCH]_0$ = 20 mg/L, $[Catalyst.]_0$ = 0.5 g/L, T = 25 °C, ambient pH, reaction time = 60 min.

3.3. Catalyst Cycling Stability Study

To investigate whether the incorporation of Mo can enhance the catalytic cycle regeneration performance, Fig. 4a-c show the results of TCH removal over multiple cycles using the catalytic systems Fe/Mg@BC-Mo/PMS, Fe@BC/PMS, and Fe/Mg@BC/PMS. After two cycles with the Fe@BC/PMS system, the TCH removal rates were 59.00% and 40.42%, respectively. After four cycles with the Fe/Mg@BC/PMS system, TCH degradation rates were 83.15%, 76.35%, 65.35%, and 54.77%. The cycling removal results of the Fe/Mg@BC-Mo/PMS system indicated that, with Mo addition, the catalyst could be reused up to nine times, with TCH removal rates within 60 minutes after the 8th and 9th cycles reaching 95.00% and 87.38%, respectively. In summary, adding Mo helps maintain Fe valence states, improves TCH degradation, and prolongs the catalyst's lifespan. To assess the catalyst's stability after multiple uses, the catalyst was examined via SEM and XRD after the 8th cycle. Fig. 5a-

g show that the catalyst's surface did not develop obvious defects or changes after 8 cycles. Although the $MgFe_2O_4$ oxide on the surface decreased, Fe and Mo remained evenly and stably attached. The XRD spectrum in Fig. 4h reveals that Mo mainly exists as MoS_2, and during the reaction, $MgFe_2O_4$ and FeC_3 were consumed.

The concentration of metal ions in the solution after 60 minutes of degradation was measured using an inductively coupled plasma atomic emission spectrometer (ICP-AES). The results**[52]** indicated that the levels of Fe, Mg, and Mo ions gradually decreased as the number of cycles increased(Text S5). To prevent potential secondary pollution from ion leaching, the doping amount of MoS_2 was optimized. As shown in Fig. 3f, reducing the MoS_2 doping ratio to Fe/Mg@BC:MoS_2 = 8:1 (wt%) resulted in a TCH degradation rate of 93.62% within 2 minutes and 97.91% within 60 minutes. This approach maintained high degradation efficiency and addressed environmental concerns related to ion leaching while also lowering catalyst preparation costs.

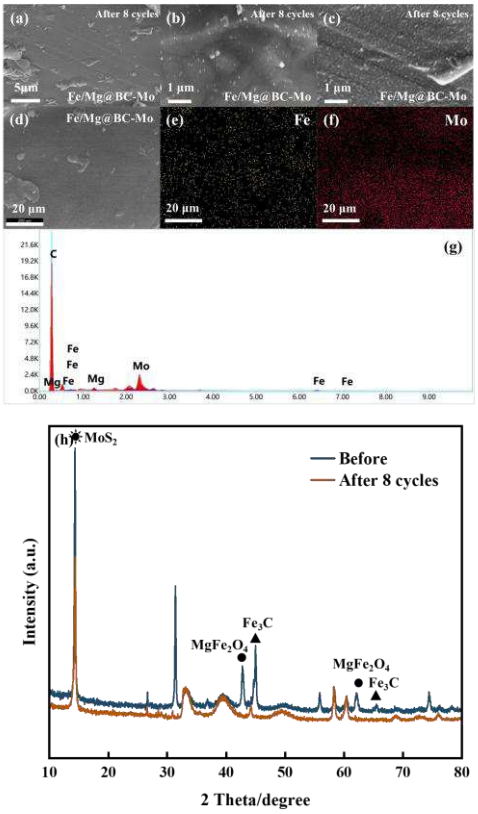


Fig.5 (a)-(c) SEM images of Fe/Mg@BC-Mo after 8 cycles of reuse; (d) EDS image; (e-f) Element mapping images; (g) Element distribution map; and (h) XRD spectrum.

3.4. Exploration of the Activation Mechanism of Fe/Mg@BC-Mo on PMS

To examine the degradation mechanism of TCH by the Fe/Mg@BC-Mo/PMS system, this study combined reactive oxygen species (ROSs) quenching experiments and electron paramagnetic resonance (EPR) analysis to identify the main types of ROS generated in the system. As shown in Fig. 4d, L-histidine (L-His), p-benzoquinone (ρ-BQ), tert-butanol (TBA), and methanol (MeOH) were chosen as quenchers for $^1O_2$, $O_2^{\cdot-}$, ·OH, and $SO_4^{\cdot-}$, respectively. Since MeOH can simultaneously quench ·OH and $SO_4^{\cdot-}$, the degradation rate dropped from 98.22% to 63.99% within 2 minutes, demonstrating the most substantial quenching effect. Additionally, after 2 minutes, the degradation rates of each group with L-His, ρ-BQ, and TBA were 76.17%, 83.84%, and 77.39%, respectively. Because TBA reacts preferentially with ·OH to combine with MeOH for quenching, this indicates the presence of both ·OH and $SO_4^{\cdot-}$ active free radicals in the catalytic system, with the higher degradation rate suggesting that more ·OH is generated. Furthermore, the production of $O_2^{\cdot-}$ in the system is relatively low and may react with other substances during later stages of degradation, leading to its consumption, while $^1O_2$ and ·OH are the main contributors to degradation. Further analysis of ROS produced in the Fe/Mg@BC-Mo/PMS system via EPR, as shown in Fig. 4e-f, used 5,5-dimethyl-1-pyrroline-N-oxide (DMPO) to trap ·OH and $SO_4^{\cdot-}$, revealing significant signal peaks and confirming that the Fe/Mg@BC-Mo/PMS system generates abundant ·OH and $SO_4^{\cdot-}$ active free radicals, consistent with the quenching results. When using 2,2,6,6-tetramethylpiperidine-1-oxide (TEMP) as the trap for $^1O_2$, the spectral lines displayed three symmetrical (1:1:1) peaks of equal intensity, indicative of typical nitrogen-oxygen free radical triplet peaks**[25]**, signifying that the Fe/Mg@BC-Mo/PMS system produces abundant non-radical active components $^1O_2$, aligning with the quenching findings.

The elemental composition and chemical state of the catalyst surface before and after the Fe/Mg@BC-Mo reaction were analyzed using XPS, as shown in Fig. 6a and d. The proportion of C-OH decreased, while the proportion of C=O increased after the reaction, indicating that the active functional group C-O on the catalyst may be oxidized to C=O to activate PMS**[53]-[54]**. In the Fe 2p XPS spectrum (Fig. 6b and e), the primary peak of Fe $2p_{3/2}$ appeared at 711.43 eV, along with a characteristic peak at 724.86 eV and distinct satellite peaks at 718.56 eV and 732.11 eV**[55]**. The binding energy data indicated that the catalyst mainly contained Fe^{3+} in the form of Fe^{3+}, with an element proportion of 75.04%. After the reaction, the binding energy values of Fe $2p_{3/2}$ and Fe $2p_{1/2}$ peaks were 711.33 eV and 724.61 eV, respectively, and the proportion of Fe^{3+} increased to 79.03%. This suggests that both Fe^{2+} and Fe^{3+} are present in the catalyst system, and Fe^{2+} is oxidised to Fe^{3+} during PMS activation. Fig. 6c and f show the Mo 3d XPS spectra, which indicate that Mo^{4+} mainly exists as MoS_2 with a small amount of oxide both before and after the reaction. The proportion of Mo^{4+} decreased from 90.64% to 88.67%, while Mo^{6+} increased from 9.36% to 11.32%. The changes in Fe^{3+} further confirmed that the incorporation of MoS_2 facilitated the transformation of Fe's valence state**[56]**. The synergistic effect of Fe^{2+}/Fe^{3+} and Mo^{4+}/Mo^{6+} efficiently and quickly enabled the activation and degradation of TCH by PMS**[57]**.

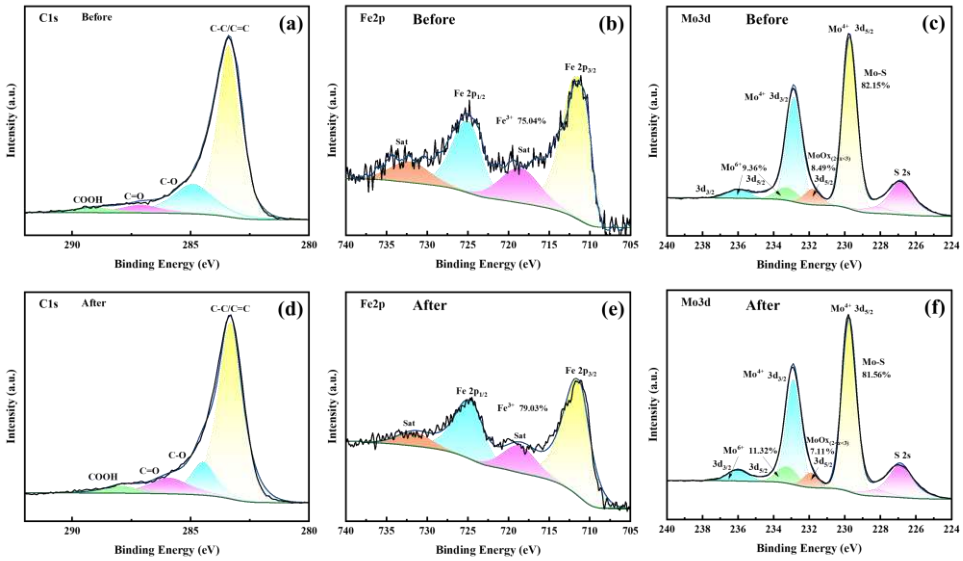


Fig.6 XPS spectra of Fe/Mg@BC-Mo, before and after catalyst use (a) and (d) C1s images; (b) and (e) Fe2p images; (c) and (f) Mo3d images.

Based on the investigation above, the mechanism by which Fe/Mg@BC-Mo activates PMS is inferred as follows (Fig. 7): The Fe and Mg ions form a complex called magnesium ferrite ($MgFe_2O_4$) and are evenly and stably attached to the biochar substrate. The Fe^{2+} on the catalyst surface is activated through electron transfer to activate PMS, producing ·OH and $SO_4^{\cdot-}$, while Fe^{2+} can also react with O_2 to generate $O_2^{\cdot-}$ (Equations 7-8). The doping of MoS_2 effectively enhances the cycling of iron valence states, and the Mo^{4+} on the catalyst surface can supply electrons to Fe^{3+} to facilitate the reduction and regeneration of Fe^{2+} (Equation 9). According to reports, MoS_2 can activate PMS to generate reactive oxygen species, thereby degrading pollutants (Equations 10-11)**[30]**. In the system, a large amount of $SO_4^{\cdot-}$ can quickly react to form ·OH, and ·OH can react with $O_2^{\cdot-}$ to produce $^1O_2$. Additionally, the oxidised Mo^{6+} can also generate some $^1O_2$ with $O_2^{\cdot-}$ (Equations 12-14)**[31]**. Based on the above analysis, $MgFe_2O_4$ allows Fe to be stably and evenly attached to the bio-based substrate, preventing the agglomeration phenomenon that may occur in many studies when loading nano Fe^0 and reducing the risk of metal ion leaching**[23]**. The synergistic effect of Fe^{2+}/Fe^{3+} and Mo^{4+}/Mo^{6+} produces abundant reactive oxygen species, enabling the catalytic system to perform efficiently while enhancing the catalyst's cycle life.

$$Fe^{2+} + HSO_5^- \rightarrow Fe^{3+} + SO_4^{\cdot-} + \cdot OH \quad (7)$$

$$Fe^{2+} + O_2 \rightarrow Fe^{3+} + O_2^{\cdot-} \quad (8)$$

$$Fe^{3+} + e^- \rightarrow Fe^{2+} \quad (9)$$

$$\equiv Mo(IV)S_2 + HSO_5^- \rightarrow \equiv Mo(V)S_2 + SO_4^{2-} + \cdot OH \quad (10)$$

$$\equiv Mo(IV)S_2 + HSO_5^- \rightarrow \equiv Mo(V)S_2 + SO_4^{\cdot-} + OH^- \quad (11)$$

$$SO_4^{\cdot-} + OH^- \rightarrow SO_4^{2-} + \cdot OH \quad (12)$$

$$\cdot OH + O_2^{\cdot-} \rightarrow {}^1O_2 + OH^- \quad (13)$$

$$Mo^{6+} + O_2^{\cdot-} \rightarrow {}^1O_2 + Mo^{4+} \quad (14)$$

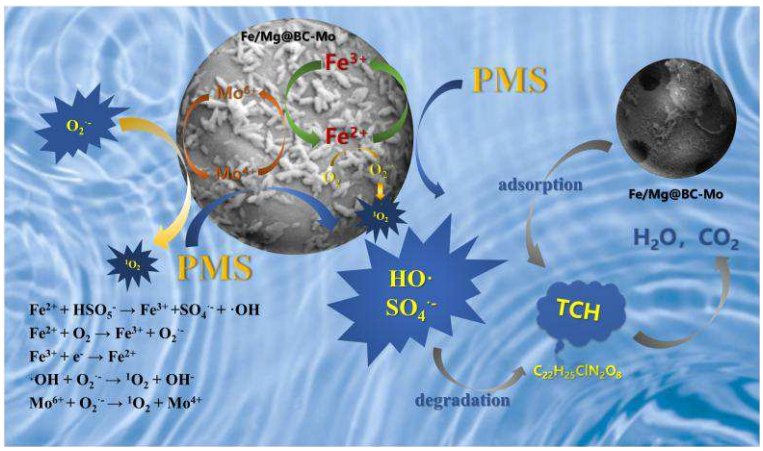


Fig.7 Mechanism of Reactive Oxygen Production and Organic Matter Degradation.

To further clarify the catalytic performance benefits of the Fe/Mg@BC-Mo system, electrochemical tests**[58]** were used to compare the linear sweep voltammogram (LSV) curves (Fig. 8a) and current-time (I-t) curves (Fig. 8b) of various catalytic materials, including Fe@BC, Fe/Mg@BC, and Fe/Mg@BC-Mo. The electrochemical results showed that the Fe/Mg@BC-Mo catalyst had the strongest current response at different potentials, and the bimetallic loading outperformed the single-metal Fe loading. This suggests that doping with Mo yields the highest electrocatalytic activity, and the rapid increase in charge transfer rate can enhance PMS activation for TCH degradation. Furthermore, the results of ongoing changes over time for various catalytic components under a constant voltage show that, compared to the Fe@BC and Fe/Mg@BC systems, the low current density in the Fe/Mg@BC-Mo system may be due to a lack of active sites on the catalyst surface. The initial current of the Fe/Mg@BC-Mo system is the highest, indicating that the catalyst has excellent reaction kinetics, which is related to the fact that the catalyst surface has more active sites for rapid mass transfer**[59]**. The current in the Fe/Mg@BC-Mo/PMS system slightly decreases during the first two minutes. Then it remains nearly constant in the plateau region, maintaining a high and stable steady-state current. Generally, the stability and decay rate of the current reflect the electrochemical stability and durability of the material. This further highlights the advantages of the Fe/Mg@BC-Mo catalytic system in degrading TCH under various conditions.

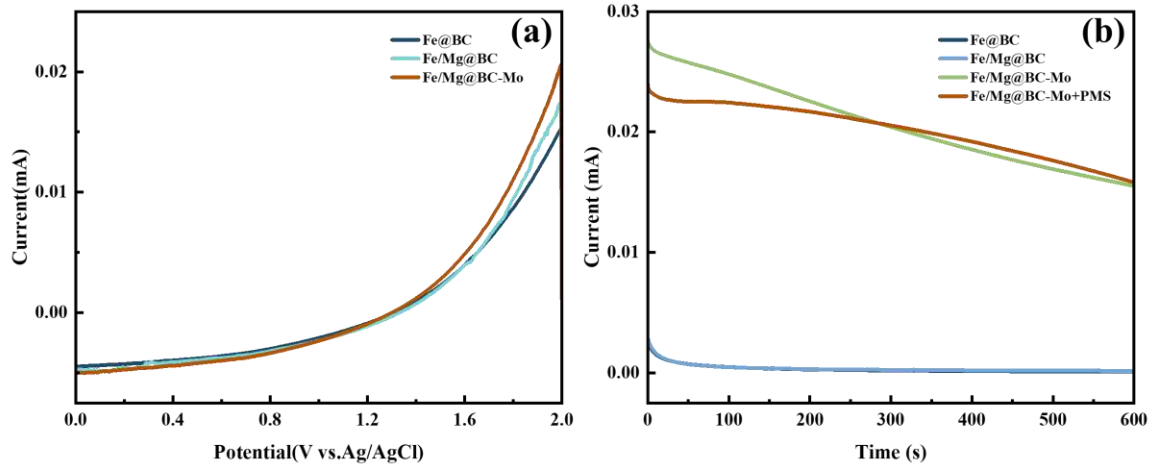


Fig.8 (a) The linear sweep voltammetry curves for Fe@BC, Fe/Mg@BC, and Fe/Mg@BC-Mo; and (b) The corresponding I-t curves. Conditions: [PMS] = 0.5 mM.

3.5. Analysis of TCH Degradation Pathway

The experiment utilised a high-performance liquid chromatography-mass spectrometry (HPLC-MS) system to identify the intermediate products of TCH degradation within the catalytic system within 60 minutes and propose possible degradation pathways**[60]**. The mass spectra of TC and its degradation intermediates are shown in Fig. S1. Fig. 9 shows four potential degradation pathways based on the mass spectrometry results. Since H^+ and Cl^- are present in the aqueous solution in ionic form, the complete hydrolysis of tetracycline hydrochloride TCH produces tetracycline TC. Therefore, the mass-to-charge ratio (m/z) of TC before degradation was P0 = 445**[61]**. During the degradation process, 13 intermediate products were detected, with m/z values of 477, 434, 412, 408, 392, 350, 304, 301, 279, 192, 163, 135, 115. In pathway I, TC first undergoes demethylation, deamidation, and breaks the C=C double bond to undergo hydroxy addition and transform into P1 (m/z = 392). Then, it undergoes deamidation and ring-opening reactions to generate P2 (m/z = 350) and further dehydroxylation to form P3 (m/z = 304). In pathway II, TC first undergoes deamidation and dehydroxylation to produce P4 (m/z = 412), then experiences a series of demethylation, deamidation, -CHO removal, and ring-opening reactions to form P5 (m/z = 301). In degradation pathway III, one -CH_3 group is removed, and a hydroxyl addition reaction occurs to produce P6 (m/z = 434). Then, another methyl group is removed, and deamidation takes place to convert it into P7 (m/z = 408). This is followed by deamidation, dihydroxylation, and ring-opening reactions to form P8 (m/z = 279). Further removal of the ortho-phenolic hydroxyl group leads to P9 (m/z = 192), which is ultimately broken down into CO_2 and H_2O**[62]** in pathways I and II, along with intermediate products P10 (m/z = 163), P11 (m/z = 135), and P12 (m/z = 115) that undergo further decomposition. Additionally, in pathway IV, TC is attacked by ·OH, leading to hydroxy addition and hydrogen removal reactions that produce -OH and -C=O-, converting P0 into P13 (m/z = 477). This explains the slight increase in the mass-to-charge ratio of some intermediate products during the degradation process.

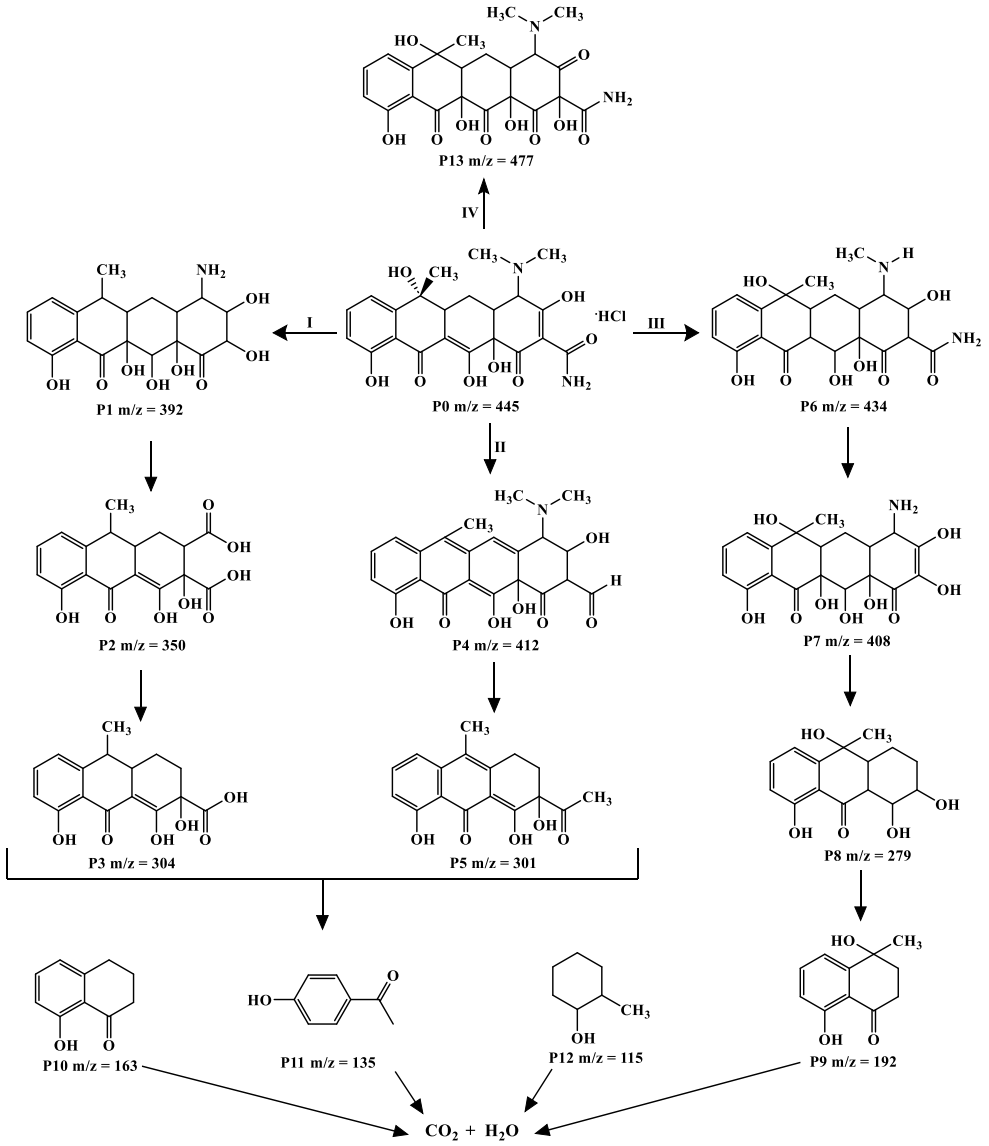


Fig.9 Possible degradation pathways of TCH in the Fe/Mg@BC-Mo system.

4. Conclusions

This study used high-temperature carbonization to produce biochar and created a biochar-based catalyst, Fe/Mg@BC-Mo, through a simple impregnation-thermal decomposition process, for activating PMS to break down TCH. Due to the large specific surface area and abundant pore structure of the catalyst Fe/Mg@BC-Mo, it provided more active sites for PMS adsorption and activation. The results showed that the Fe/Mg@BC-Mo/PMS system could degrade 98.22% of TCH in just 2 minutes, significantly reducing the time needed for pollutant removal. The catalyst exhibits recyclability, maintaining effective performance over multiple cycles. After nine recycling iterations, the catalytic system achieved a tetracycline hydrochloride degradation rate of 87.38%. It maintained effective catalytic activity even under various conditions, including a wide pH range, different anions, and varying pollutant concentrations. Moreover, the uniform and stable dispersion of Fe and Mg within complex oxide crystals on the catalyst surface could reduce metal ion leaching, addressing potential environmental pollution. In summary, Fe/Mg@BC-Mo is an eco-friendly catalyst that effectively activates PMS to degrade TCH, improves catalyst recyclability, and allows quick separation and recovery using magnetic components.

Author contributions

Haifeng Li: Conceptualization, Data curation, Formal analysis, Investigation, Methodology, Resources, Visualization, Writing – original draft. **Yu Yao:** Investigation, Methodology, Resources. **Peixuan Li:** Methodology. **Xiqian Guo:** Data curation. **Yan Zhang:** Conceptualization, Funding acquisition, Writing – review & editing. **Jifen Wang:** Funding acquisition. **Yi Zhang:** analysis and validation. All authors reviewed the manuscript.

Funding

The National Natural Science Foundation of China (No. 51776116, 52176081) and Shanghai Science and Technology Project (No.

22010500600) and sponsored by Shanghai Sailing Program (No.19YF1416500).

Data availability statements

The data that support the findings of this study are available from the corresponding author upon reasonable request.

Declarations

Competing Interests The authors declare no competing interests.

Ethical Approval Not applicable.

Consent To Participate Informed consent.

Consent for Publication Not applicable.

Acknowledgements

This work is supported by the National Natural Science Foundation of China (No. 51776116, 52176081) and Shanghai Science and Technology Project (No. 22010500600) and sponsored by Shanghai Sailing Program (No.19YF1416500).

References

1. Wilkinson JL, Boxall ABA, Kolpin DW, et al (2022) Pharmaceutical pollution of the world's rivers[J]. Proceedings of the National Academy of Sciences of the United States of America1, 19:e2113947119. https://doi.org/10.1073/pnas.2113947119

2. Lozano I, Pérez-Guzmán CJ, Mora A, et al (2022) Pharmaceuticals and personal care products in water streams: Occurrence, detection, and removal by electrochemical advanced oxidation processes[J]. Science of The Total Environment, 827:154348. https://doi.org/10.1016/j.scitotenv.2022.154348

3. Wei T, Song X, Zhang J, et al (2024) Efficient adsorption of tetracycline hydrochloride by Willow Catkins based biochar: Performance, governing factors and mechanisms[J]. Biomass Conversion and Biorefinery, 14:18761–18773. https://doi.org/10.1007/s13399-023-04146-4

4. Kulkarni SR, Nighojkar A, Kandasubramanian B (2023) Aqueous Adsorption of Pharmaceutical Pollutants on Biochar: a Review on Physicochemical Characteristics, Classical Sorption Models, and Advancements in Machine Learning Techniques[J]. Water Air Soil Pollut 234:684. https://doi.org/10.1007/s11270-023-06696-9

5. Chatterjee A, Jana AK, Basu JK (2021) A binary MOF of iron and copper for treating ciprofloxacin-contaminated waste water by an integrated technique of adsorption and photocatalytic degradation[J]. New J Chem 45:17196–17210. https://doi.org/10.1039/D1NJ02880D

6. Ayoub M (2022) Degradation of tetracycline using nanoparticles of zero-valent iron and copper[J]. Water Practice and Technology 17:246–253. https://doi.org/10.2166/wpt.2021.100

7. Lee J, Von Gunten U, Kim J-H (2020) Persulfate-Based Advanced Oxidation: Critical Assessment of Opportunities and Roadblocks[J]. Environ Sci Technol 54:3064–3081. https://doi.org/10.1021/acs.est.9b07082

8. Butt MT, Yin H (2024) Effective removal of chromium, copper, and nickel heavy metal ions from industrial electroplating wastewater by in situ oxidative adsorption using sodium hypochlorite as oxidant and sodium trititanate nanorod as adsorbent[J]. Chinese Journal of Chemical Engineering 74:312–330. https://doi.org/10.1016/j.cjche.2024.06.014

9. Zhao K, Padervand M, Ren H, et al (2024) Enhancing Tetracycline Removal Efficiency through Ozone Micro–Nano Bubbles: Environmental Implication and Degradation Pathway[J]. ACS EST Eng 4:1860–1870. https://doi.org/10.1021/acsestengg.4c00102

10. Gómez-Pacheco CV, Sánchez-Polo M, Rivera-Utrilla J, López-Peñalver J (2011) Tetracycline removal from waters by integrated technologies based on ozonation and biodegradation[J]. Chemical Engineering Journal 178:115–121. https://doi.org/10.1016/j.cej.2011.10.023

11. Su Y, Wang X, Dong S, et al (2020) Towards a simultaneous combination of ozonation and biodegradation for enhancing tetracycline decomposition and toxicity elimination[J]. Bioresource Technology 304:123009. https://doi.org/10.1016/j.biortech.2020.123009

12. Sun Z, Wei Q, Hua W, et al (2024) Engineered biochar for advanced oxidation process towards tetracycline degradation: Role of iron and graphitic structure[J]. Journal of Environmental Chemical Engineering 12:114290. https://doi.org/10.1016/j.jece.2024.114290

13. Song W, Li J, Wang Z, Zhang X (2019) A mini review of activated methods to persulfate-based advanced oxidation process[J]. Water Science and Technology 79:573–579. https://doi.org/10.2166/wcc.2018.168

14. Xiao H, Wang Y, Lv K, et al (2025) N-doped biochar-Fe/Mn as a superior peroxymonosulfate activator for enhanced bisphenol a degradation[J]. Water Research 278:123399. https://doi.org/10.1016/j.watres.2025.123399

15. Potakis N, Frontistis Z, Antonopoulou M, et al (2017) Oxidation of bisphenol A in water by heat-activated persulfate[J]. Journal of Environmental Management 195:125–132. https://doi.org/10.1016/j.jenvman.2016.05.045

16. Huang M, Wang X, Zhu C, et al (2022) Efficient chlorinated alkanes degradation in soil by combining alkali hydrolysis with

thermally activated persulfate[J]. Journal of Hazardous Materials 438:129571. https://doi.org/10.1016/j.jhazmat.2022.129571

17. Lou X, Fang C, Geng Z, et al (2017) Significantly enhanced base activation of peroxymonosulfate by polyphosphates: Kinetics and mechanism[J]. Chemosphere 173:529–534. https://doi.org/10.1016/j.chemosphere.2017.01.093

18. Zhou L, Ferronato C, Chovelon J-M, et al (2017) Investigations of diatrizoate degradation by photo-activated persulfate[J]. Chemical Engineering Journal 311:28–36. https://doi.org/10.1016/j.cej.2016.11.066

19. Gao F, Li Y, Xiang B (2018) Degradation of bisphenol A through transition metals activating persulfate process[J]. Ecotoxicology and Environmental Safety 158:239–247. https://doi.org/10.1016/j.ecoenv.2018.03.035

20. Wacławek S, Lutze HV, Grübel K, et al (2017) Chemistry of persulfates in water and wastewater treatment: A review[J]. Chemical Engineering Journal 330:44–62. https://doi.org/10.1016/j.cej.2017.07.132

21. Feng X, Chen H, Guo S, et al (2025) Fe0-modified sulfur-rich vacancy CoS2 enhanced persulfate photoactivation: Achieving high surface adsorption and rapid degradation of antibiotics[J]. Separation and Purification Technology 356:129864. https://doi.org/10.1016/j.seppur.2024.129864

22. Chen J, Zhan Z, Chen Z, et al (2024) Ultrasound synergistic iron-nitrogen biocarbon activated persulfate to ofloxacin degradation[J]. Journal of Environmental Chemical Engineering 12:112759. https://doi.org/10.1016/j.jece.2024.112759

23. Rahmati R, Mai A, Christodoulatos C, et al (2024) Impact of operational parameters on degradation of nitroglycerin using biochar doped with nano zerovalent iron[J]. Journal of Environmental Chemical Engineering 12:114911. https://doi.org/10.1016/j.jece.2024.114911

24. Murugesan C, Aroutchelvane J, Okrasa L, Chandrasekaran G (2018) Synthesis and Characterisation of Superparamagnetic $MgFe_2O_4$ Nanoferrite[J]. J Supercond Nov Magn 31:3255–3262. https://doi.org/10.1007/s10948-018-4573-3

25. Chen L, Jiang X, Xie R, et al (2020) A novel porous biochar-supported Fe-Mn composite as a persulfate activator for the removal of acid red 88[J]. Separation and Purification Technology 250:117232. https://doi.org/10.1016/j.seppur.2020.117232

26. Liu J, Zhu J, Ma X, et al (2025) Cerium-regulated Mg3FeO4@biochar activated persulfate to enhance degradation of aqueous tetracycline: The dominant role of cerium[J]. Applied Surface Science 680:161416. https://doi.org/10.1016/j.apsusc.2024.161416

27. Scaggiante G, Checa-Fernandez A, Zingaretti D, et al (2024) Activation of peroxydisulfate and peroxymonosulfate by zero-valent iron and FeCu bimetals for 4-chlorophenol oxidation in water[J]. Journal of Water Process Engineering 68:106446. https://doi.org/10.1016/j.jwpe.2024.106446

28. Liang Y, Tao R, Zhao B, et al (2024) Roles of iron and manganese in bimetallic biochar composites for efficient persulfate activation and atrazine removal[J]. Biochar 6:41. https://doi.org/10.1007/s42773-024-00331-4

29. Yu X, Wang Y, Long X, et al (2024) Effective degradation of recalcitrant naphthenic acids by the Fe(III)/peroxymonosulfate oxidation enhanced by molybdenum disulfide: Degradation performance and mechanisms[J]. Journal of Environmental Chemical Engineering 12:112842. https://doi.org/10.1016/j.jece.2024.112842

30. Li L, Guo J, Zheng K, et al (2024) MoS_2-mediated active hydrogen modulation to boost Fe^{2+} regeneration in solar-driven electro-Fenton process[J]. Journal of Hazardous Materials 470:134274. https://doi.org/10.1016/j.jhazmat.2024.134274

31. Li L, Wang W, Shen Z, et al (2025) Trimetallic synergy of Fe-Co-Mo cathode for efficient non-radical degradation in a heterogeneous photo-electro-Fenton process[J]. Chemical Engineering Journal 506:159890. https://doi.org/10.1016/j.cej.2025.159890

32. Ma H, Ai J, Lu C, Christian Bruun Hansen H (2022) Element doping of biochars enhances catalysis of trichloroethylene dechlorination[J]. Chemical Engineering Journal 428:132496. https://doi.org/10.1016/j.cej.2021.132496

33. Faria AJGD, Rufini M, Leite ADA, et al (2021) Elemental analysis of biochar-based fertilizers via portable X-ray fluorescence spectrometry[J]. Environmental Technology & Innovation 23:101788. https://doi.org/10.1016/j.eti.2021.101788

34. Kitamura N, Konishi Y, Ma W, et al (2022) Positive-electrode properties and crystal structures of mg-rich transition metal oxides for magnesium rechargeable batteries[J]. Scientific Reports 12:18097. https://doi.org/10.1038/s41598-022-23022-1

35. Nguyen V-T, Nguyen T-B, Chen C-W, et al (2019) Influence of pyrolysis temperature on polycyclic aromatic hydrocarbons production and tetracycline adsorption behavior of biochar derived from spent coffee ground[J]. Bioresource Technology 284:197–203. https://doi.org/10.1016/j.biortech.2019.03.096

36. Zhao C, Ma J, Li Z, et al (2020) Highly enhanced adsorption performance of tetracycline antibiotics on KOH-activated biochar derived from reed plants[J]. RSC Adv 10:5066–5076. https://doi.org/10.1039/C9RA09208K

37. Li B, Zhang Y, Xu J, et al (2021) Simultaneous carbonization, activation, and magnetization for producing tea waste biochar and its application in tetracycline removal from the aquatic environment[J]. J Environ Chem Eng 9:105324. https://doi.org/10.1016/j.jece.2021.105324

38. Zhang H, Song X, Zhang J, et al (2022) Performance and mechanism of sycamore flock based biochar in removing oxytetracycline hydrochloride[J]. Bioresour Technol 350:126884. https://doi.org/10.1016/j.biortech.2022.126884

39. Shen Q, Wang Z, Yu Q, et al (2020) Removal of tetracycline from an aqueous solution using manganese dioxide modified biochar derived from chinese herbal medicine residues[J]. Environmental Research 183:109195. https://doi.org/10.1016/j.envres.2020.109195

40. Tao W, Duan W, Liu C, et al (2020) Formation of persistent free radicals in biochar derived from rice straw based on a detailed analysis of pyrolysis kinetics[J]. Sci Total Environ 715:136575. https://doi.org/10.1016/j.scitotenv.2020.136575

41. Feng S, Yu M, Xie T, et al (2022) MoS2/CoFe2O4 heterojunction for boosting photogenerated carrier separation and the dominant role in enhancing peroxymonosulfate activation[J]. Chem Eng J 433:134467. https://doi.org/10.1016/j.cej.2021.134467

42. Ji J, Xu S, Ma Z, Mou Y (2022) Trivalent antimony removal using carbonaceous nanomaterial loaded with zero-valent bimetal (iron/copper) and their effect on seed growth[J]. Chemosphere 296:134047. https://doi.org/10.1016/j.chemosphere.2022.134047

43. Liu J, Luo K, Li X, et al (2020) The biochar-supported iron-copper bimetallic composite activating oxygen system for simultaneous adsorption and degradation of tetracycline[J]. Chem Eng J 402:126039. https://doi.org/10.1016/j.cej.2020.126039

44. Zhao Z, Zhai X, Shao W, et al (2023) Activation of peroxymonosulfate by biochar-supported Fe3O4 derived from oily sludge to enhance the oxidative degradation of tetracycline hydrochloride[J]. J Environ Manage 347:119187. https://doi.org/10.1016/j.jenvman.2023.119187

45. Pan X, Pu J, Zhang L, et al (2024) Bimetallic iron-nickel phosphide as efficient peroxymonosulfate activator for tetracycline hydrochloride degradation: performance and mechanism[J]. Environ Res 249:118362. https://doi.org/10.1016/j.envres.2024.118362

46. Li Y, Li M, Zhu C, et al (2023) Main factors for photocatalytic degradation of rhodamine B by MoS_2 activated PMS[J]. Materials Letters 341:134191. https://doi.org/10.1016/j.matlet.2023.134191

47. Zhang Y, Zhang C, Zhou Z, et al (2021) Degradation of ciprofloxacin by persulfate activation with CuO supported on mg al layered double hydroxide[J]. J Environ Chem Eng 9:106178. https://doi.org/10.1016/j.jece.2021.106178

48. Yi C, He Z, Hu Y, et al (2021) FeOOH@MoS_2 as a highly effective and stable activator of peroxymonosulfate-based advanced oxidation processes for pollutant degradation[J]. Surf Interfaces 27:101465. https://doi.org/10.1016/j.surfin.2021.101465

49. Sun J, Zhang D, Xia D, Li Q (2023) Orange peels biochar doping with Fe-Cu bimetal for PMS activation on the degradation of bisphenol A: A synergy of $SO_4^{\cdot-}$, ·OH, $^1O_2$ and electron transfer[J]. Chemical Engineering Journal 471:144832. https://doi.org/10.1016/j.cej.2023.144832

50. Xiao M, Qi Y, Feng Q, et al (2021) P-cresol degradation through fe(III)-EDDS/H_2O_2 fenton-like reaction enhanced by manganese ion: effect of pH and reaction mechanism[J]. Chemosphere 269:129436. https://doi.org/10.1016/j.chemosphere.2020.129436

51. Zhang X, Wei J, Wang C, et al (2024) Recent advance of fe-based bimetallic persulfate activation catalysts for antibiotics removal: performance, mechanism, contribution of the key ROSs and degradation pathways[J]. Chem Eng J 487:150514. https://doi.org/10.1016/j.cej.2024.150514

52. Liu J, Zhu J, Zeng X, et al (2024) Enhanced activation of persulfate by bimetal and nitrogen co-doped biochar for efficient degradation of refractory organic contaminants: the role of the second metal[J]. Journal of Physics and Chemistry of Solids 193:112191. https://doi.org/10.1016/j.jpcs.2024.112191

53. Guo L, Zhao L, Tang Y, et al (2022) An iron–based biochar for persulfate activation with highly efficient and durable removal of refractory dyes[J]. J Environ Chem Eng 10:106979. https://doi.org/10.1016/j.jece.2021.106979

54. Tian H, Cui K, Sun S, et al (2023) Sequential doping of exogenous iron and nitrogen to prepare fe-N structured biochar to enhance the activity of OTC degradation[J]. Sep Purif Technol 322:124249. https://doi.org/10.1016/j.seppur.2023.124249

55. Li J, Lin Q, Luo H, et al (2022) The effect of nanoscale zero-valent iron-loaded N-doped biochar on the generation of free radicals and nonradicals by peroxydisulfate activation[J]. J Water Process Eng 47:102681. https://doi.org/10.1016/j.jwpe.2022.102681

56. Peng H, Chen R, Tao N, et al (2022) MoS2 boosts the Fe2 /PMS process for carbamazepine degradation[J]. Environ Sci Pollut Res 29:49267–49278. https://doi.org/10.1007/s11356-022-19172-4

57. Hu S, Li Y, Zang C, et al (2020) Piezoelectric field-promoted heterogeneous sono-fenton performance of MoS_2/α-Fe_2O_3 heterojunction structure[J]. Appl Surf Sci 534:147499. https://doi.org/10.1016/j.apsusc.2020.147499

58. Li W, Yuan C(2022) Degradation of carbon materials in electrocatalysis[J]. Current Opinion in Electrochemistry 36:101159. https://doi.org/10.1016/j.coelec.2022.101159

59. Li L, Bai J, Chen S, et al (2020) Enhanced O2− and HO via in situ generating H_2O_2 at activated graphite felt cathode for efficient photocatalytic fuel cell[J]. Chem Eng J 399:125839. https://doi.org/10.1016/j.cej.2020.125839

60. He Z, Siddique MS, Yang H, et al (2022) Novel Z-scheme In_2S_3/Bi_2WO_6 core-shell heterojunctions with synergistic enhanced photocatalytic degradation of tetracycline hydrochloride[J]. J Cleaner Prod 339:130634. https://doi.org/10.1016/j.jclepro.2022.130634

61. (2022) Efficient purification of tetracycline wastewater by activated persulfate with heterogeneous co-V bimetallic oxides[J]. J Colloid Interface Sci 619:188–197. https://doi.org/10.1016/j.jcis.2022.03.126

62. Acharya L, Nayak S, Pattnaik SP, et al (2020) Resurrection of boron nitride in p-n type-II boron nitride/B-doped-g-C_3N_4 nanocomposite during solid-state Z-scheme charge transfer path for the degradation of tetracycline hydrochloride[J]. Journal of Colloid and Interface Science 566:211–223. https://doi.org/10.1016/j.jcis.2020.01.074

Supplementary Files

This is a list of supplementary files associated with this preprint. Click to download.

- SupportingInformation.docx